RAA 2020 Vol. **20** No. **9**, 138(12pp) doi: 10.1088/1674–4527/20/9/138

http://www.raa-journal.org *http://iopscience.iop.org/raa*

***R**esearch in*
***A**stronomy and*
***A**strophysics*

Observational evidence of magnetic reconnection in a coronal bright point

Zong-Jun Ning (宁宗军), Dong Li (李东) and Qing-Min Zhang (张擎旻)

Key Laboratory of Dark Matter and Space Astronomy, Purple Mountain Observatory, Nanjing 210033, China; *ningzongjun@pmo.ac.cn*

Received 2019 December 17; accepted 2020 April 6

Abstract Magnetic reconnection is considered to be the fundamental process by which magnetic energy is converted into plasma or particle kinetic energy. Magnetic reconnection is a widely applied physics model to explain the solar eruption events, such as coronal bright points (CBPs). Meanwhile, it is an usual way of the solar physics research to look for the observational evidences of magnetic reconnection in the solar eruption events in order to support the model. In this paper, we have explored the evidences of magnetic reconnection in a CBP observed by the Atmospheric Imaging Assembly (AIA) onboard the *Solar Dynamics Observatory* (SDO) at NOAA No. 11163 on 2011 March 5. Our observations show that this event is a small-scale loop system in active regions that have similar size as a traditional CBP and it might shed light on the physics of a traditional CBP. This CBP is bright in all nine AIA wavelengths and displays a flaring development with three bursts intermittently. Each burst exhibits a pair of bi-directional jets almost along a line. They originate from the same position (CBP core), then move in the opposite directions. Our findings are well consistent with the magnetic reconnection process by which the bi-directional plasma outflows are produced and radiate the bi-directional jets detected by SDO/AIA. These facts further support the conclusion that the CBP is produced by the magnetic reconnection process.

Key words: Sun: UV radiation — Sun: corona — Sun: oscillation

1 INTRODUCTION

Magnetic reconnection suggests the process in which the magnetic lines of force break and rejoin into a lower-energy configuration rapidly. In other words, before the reconnection, the magnetic fields are located in a highly non-potential state (e.g., Petschek 1964). During the reconnection, the field lines are swept into the diffusion region and the plasma following with them are referred to reconnection inflows, while the plasma with reconfigured loops are termed reconnection outflows, which are along the opposite direction on the two-dimension space and thought to be in the same order of the local Alfvén speed. This process suggests that magnetic energy is converted into plasma or particle kinetic energy rapidly. Therefore, the magnetic reconnection is wildly used to explain the solar eruption events, such as flares (Carmichael 1964; Sturrock 1966; Hirayama 1974; Kopp & Pneuman 1976) and coronal bright points (CBPs). Observationally, it is harder to see the direct evidences of magnetic reconnection. However, the bi-directional plasma outflows can radiate emissions or produce certain instabilities or consequences on their trajectories after left reconnection region. Therefore, it is a common way to find the solar emission signatures consistent with the theory predicts of the bi-directional plasma outflows to prove the reconnection process took place on the Sun (Innes et al. 1997; Liu et al. 2013; Su et al. 2013).

CBPs are observed as the coronal brightness enhancements in X-ray, extreme ultraviolet (EUV) and radio emissions over the Sun. Previous observations show that CBPs are small roundish and compact. They have a typical size of $5'' - 10''$, and last for several hours or longer (Golub et al. 1974; Zhang et al. 2001; Cirtain et al. 2007; Kariyappa & Varghese 2008; Alexander et al. 2011; Li & Ning 2012; Li et al. 2013; Zhang et al. 2012). With high-resolution observations, it has revealed that the CBPs are actually composed of closed coronal loops, especially at soft X-rays (Sheeley & Golub 1979; Dere 2008; Kariyappa & Varghese 2008; Kariyappa et al. 2011). Ueda et al. (2010) statistically studied the CBPs with such loop-like structures and found their orientation is clearly biased to the east-west direction. The CBP lifetime is proportional to the magnetic flux of the corresponding bipoles in the photosphere as well as their area

in soft X-ray images (Golub et al. 1977). CBPs have an average lifetime of approximately 20 hours at EUV emissions (Habbal & Withbroe 1981; Scherrer et al. 1995; Zhang et al. 2001; Li & Li 2010; Li & Ning 2012), which is longer than the CBPs at soft X-rays. Observations reveal that the most of CBPs at EUV are one-to-one correspondence to the magnetic poles on the photosphere, regardless of the positive and negative polarities (Li & Ning 2012). CBPs can be observed in the radio wavelengths, such as 20 cm and 6 cm (Habbal et al. 1986; Fu et al. 1987). They found that the brightness temperature of CBPs varies between 10^4 K and 10^5 K, and the lifetime is between 5 and 20 minutes.

CBPs are theoretically thought to be produced by magnetic reconnection. Because they are found to be associated with small, opposite-polarity poles in photospheric magnetograms (Priest et al. 1994), or to be associated with the emergence of the new magnetic flux (Krieger et al. 1971; Strong et al. 1992; Golub et al. 1977; Webb et al. 1993; Podgorny & Podgorny 2000; Huang et al. 2012; Mou et al. 2016, 2018). After statistically studying CBPs and their related magnetic fields on the photosphere, Harvey et al. (1994) found that CBPs tend to occur at the regions with magnetic bipolar emerging, canceling or emerging then canceling. These observations strongly support that CBP is a consequence produced by magnetic reconnection due to the interaction between two opposite magnetic fragments. So far, there are three typical models explaining the CBPs, such as the converging-flux model (e.g., Priest et al. 1994), the separator reconnection model (Longcope et al. 2001; Madjarska et al. 2003) and the new emergence-flux model (Shibata et al. 1992, 1994, 2007; Yokoyama & Shibata 1995; Moore et al. 2010; Fang et al. 2014). Their basic idea is the magnetic reconnection process. However, the first model emphasizes the photosphere converging motion contribution to the magnetic reconnection, while the second one focuses on the shear motion of the magnetic fields. The third model suggests the reconnection between the new emergence-flux and pre-existing fields to explain the CBPs. This magnetic reconnection model is used to explain not only the CBPs with a stable pattern for a long lifetime but also those with the flashes or the flaring events accompanying the bi-directional bright structures. Based on the two-dimensional reconnection model, the bi-directional bright structures are expected as the observational evidences of the bi-directional plasma outflows (Shibata et al. 1992, 1994; Shimojo et al. 1996; Ning & Guo 2014; Li et al. 2016).

Based on the observations with high resolutions, it is found that CBPs evolve in an active manner (Huang et al. 2018; Mou et al. 2016; Mou et al. 2018; Skokić et al. 2019). Some occasionally undergo a sudden increase in emissions such as flashes on a typical time scale of several minutes, like solar flares (Habbal & Withbroe 1981; Habbal et al. 1990; Strong et al. 1992; Koutchmy et al. 1997; Zhang et al. 2012). These flashes show many subpeaks on the light curves, and they often behave quasi-periodically with the timescale of a few or tens of minutes (Tian et al. 2008; Kariyappa & Varghese 2008; Zhang et al. 2012). Imaging observations suggest that these brightness flashes are consistent with the jets at X-ray or EUV emissions (Shibata et al. 1992; Yokoyama & Shibata 1995; Shimojo et al. 1996; Chae et al. 1999; Pariat et al. 2009; Zhang et al. 2012; Huang et al. 2019a). A gigantic jet associated with CBP is observed by soft X-ray telescope on board YOHKOH (Shibata et al. 1994). The jet velocities is from 90 to 240 km s^{-1}, which is corresponding to a kinetic energy estimated to be order of 10^{28} ergs. Sometimes, such eruptive behavior is thought to be the microflare associated with CBPs (e.g., Kamio et al. 2011). Meanwhile, in contrast to the traditional CBPs, which are the coronal compact brightenings in coronal holes or quiet Sun regions, CBPs are also found with the fine structures in active regions thanks to the high resolution observations of recent years. For example, CBPs consist of multi-thermal loop system that are also frequently seen in active regions with similar size (e.g., Huang 2018; Huang et al. 2019b); The intensity variations in CBPs can also be seen in loops with similar size in active regions (e.g., Huang et al. 2019b); CBPs can also produce mini-CMEs that might have a similar mechanism as large scale CMEs in active regions (e.g., Innes et al. 2009, 2010). In this paper, we will analyze an EUV CBP in active region detected by the Atmospheric Imaging Assembly (AIA) onboard the *Solar Dynamics Observatory* (SDO/AIA; Lemen et al. 2012) to present the observational evidences of the magnetic reconnection.

2 OBSERVATIONS

SDO/AIA provides multi-wavelength and full-disk solar imaging capability for spatially investigating the CBPs in detail thanks to the high temporal and spatial resolutions from the chromosphere to corona. AIA has a spatial resolution of $0.6''$ and a temporal resolution of 24 s at 1700 Å and 1600 Å, while 12 s at other seven channels, such as 304 Å, 211 Å, 193 Å, 131 Å, 171 Å, 94 Åand 335 Å. The data used in this paper are detected by SDO/AIA at solar Active Region No. 11163 from 02:30 to 03:30 UT on 2011 March 5. There are several EUV CBPs occurrences during this interval. One of them has a central position at $[542'', 390'']$, and it is studied here in detail. Figure 1 gives AIA 171 Å images at 02:40 UT (a) and 02:45 UT (b) respectively. This CBP starts to be bright at 02:35 UT, then continuously expand from its core ($[542'', 390'']$) marked by the red plus.

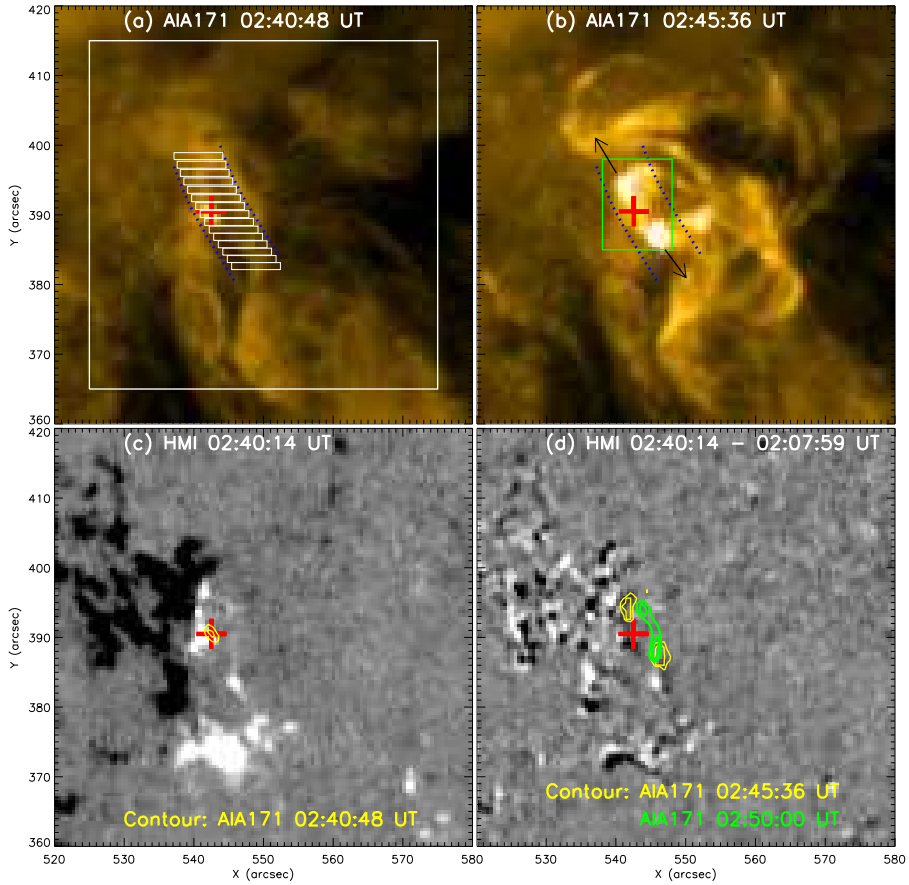

Fig. 1 SDO/AIA 171 Å images at 02:40:48 UT (a) and 02:45:36 UT (b) on 2011 March 5, SDO/HMI magnetogram at 02:40:14 UT (c) and the difference HMI image (d) between 02:40:14 UT and 02:07:59 UT with AIA 171 Å contours. The levels are set at 70% and 90% of local maximum brightness each image. Two *blue dotted lines* represent the artificial slit with a width of $8''$. The *arrows* are along the jet direction, while the *red plus* marks the core position of the CBP. The light curves in the *white* and *green boxes* are given in Fig. 2. The *white rectangles* present the 15 distinct regions in which AIA brightness used to detect the local temperature and emission measure given in Figs. 6 and 7. Each *rectangle* has a size of 8×1 arcsec^2.

There are two jets from the CBP core at 02:45 UT, and there is a distance of about $10''$ between them. Panel (c) is the Helioseimic and Magnetogram Images (HMI) photosphere magnetic field at 02:40 UT. The CBP takes place near the neutral line between the positive and negative magnetic fields. Panel (d) shows the difference image of HMI observations between 02:40 UT and 02:07 UT after removing the differential rotation. The contours of AIA 171 Å are overplotted at 02:40 UT (yellow) and 02:50 UT (green), at which a thermal loop structure appears.

Figure 2 shows the AIA light curves of the whole active region (upper panel) in the white box and of the burst area (bottom) in the green box in Figure 1. There is only one emission enhancement or flash after 02:41 UT, especially at AIA 94 Å from the whole active region. However, the bottom panel shows that the CBP firstly increase it AIA intensities at about 02:35 UT, then twice brightness enhancements after 02:41 UT. These three flashes are identified as three bursts during the time interval between 02:30 UT and 03:08 UT. They are marked by Roman numerals of I, II, and III (the blue intervals). Their lifetimes and brightness are different from the various AIA wavelengths. The second and third bursts are mixed up on the AIA channels with the higher temperature due to a short interval between them, such as AIA 131 Å and AIA 94 Å.

SDO/AIA provides the abilities for the image studying the time evolution of this CBP with a high cadence. Figure 3 gives the time sequences of intensity images and intensity gradient (running difference) images for the second burst at AIA 171 Å and 211 Å during a short interval from 02:40:24 UT to 02:41:48 UT. These images show that the CBP starts with a small roundish and compact point at the position of $[542'', 390'']$, i.e., 02:40:24 UT. Then CBP becomes more bright and expands to 25 pixels (9 arcsec^2) until 02:41:00 UT. The CBP changes its shape into a strip-type along the northeast to southwest direction

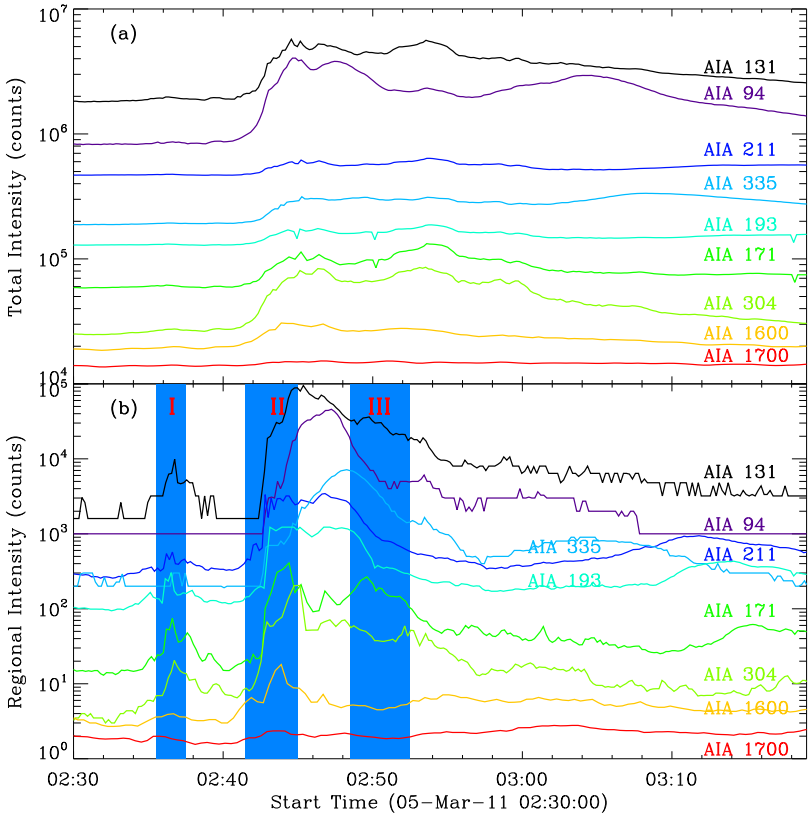

Fig. 2 Light curves of the whole active region (*upper*: the *white box* in Fig. 1) and the CBP (*bottom*: the *green box*) region at AIA nine wavelengths. Three *blue intervals* marked by Roman numbers of I, II and III represent three bursts corresponding to three pairs of bi-directional jets.

from a roundish point after 02:41:12 UT. Its central position shifts one arcsec to west, from [542″, 390″] to [543″, 390″]. At this time, the bi-directional jets start to move out from the CBP core along the northeast-southwest direction. But they are hard to be seen by eyes from the intensity image at 02:41:12 UT. This is because a short distance separation between them. After 24 seconds, the bi-directional jets move oppositely and could have a large distance to separate them. However, it is still hard to see the jets on the raw intensity images, whatever at AIA 171 Å or 211 Å. The CBP still shows its brightness with a strip-type shape at 02:41:36 UT. However, the bi-directional jets and their movement can be clearly seen by eyes on the running difference image. On these images, each jet is represented by a pair of bright and dark kernels. The white kernel suggests the position to be bright at this time, while the dark one indicates the position to be bright previously. In this case, the white kernel has to be followed by the dark one on the running difference images, and both kernels change their positions simultaneously. This fact provides observational evidences of the jet movement. At 02:41:36 UT, the CBP shows two dark and three bright kernels (marked by three arrows in Fig. 3) along the northeast-southwest direction on the running difference image at AIA 211 Å. The green arrow points the white kernel located at the CBP core at [543, 390]. It is the newly bright region of the CBP at this time. Other two dark and bright kernels (white arrows) are symmetrically sited around the CBP core along the northeast-southwest direction. In other words, two white kernels are at the outsides of two dark kernels, and these two dark kernels are at the outsides of the CBP core. Such distribution of these kernels indicates that the two jets move outwards from the CBP core along the opposite directions. Namely, both jets are symmetrically located at the outsides of the CBP core, and they show a similar behavior.

To show the bi-directional jets in detail, we outline the CBP along an artificial slit as two blue dotted lines (in Figs. 1 and 3). In this paper, a constant width of $8''$ is used for this slit, which is wide enough to cover the whole CBP brightness at different channels and times. This slit is long enough to cover the maximum distance that the jets can reach. As mentioned before, the bi-directional jets are along the northwest-southeast direction, thus the slit is nearly a straight line. Then, the CBP brightness are integrated along the slit width from 02:30 UT to 03:08 UT. Thus, we obtain the time-distance images of CBP brightness. Figure 4 (left) shows these time-distance images at nine AIA wavelengths. The Y-axis shows the distance a-

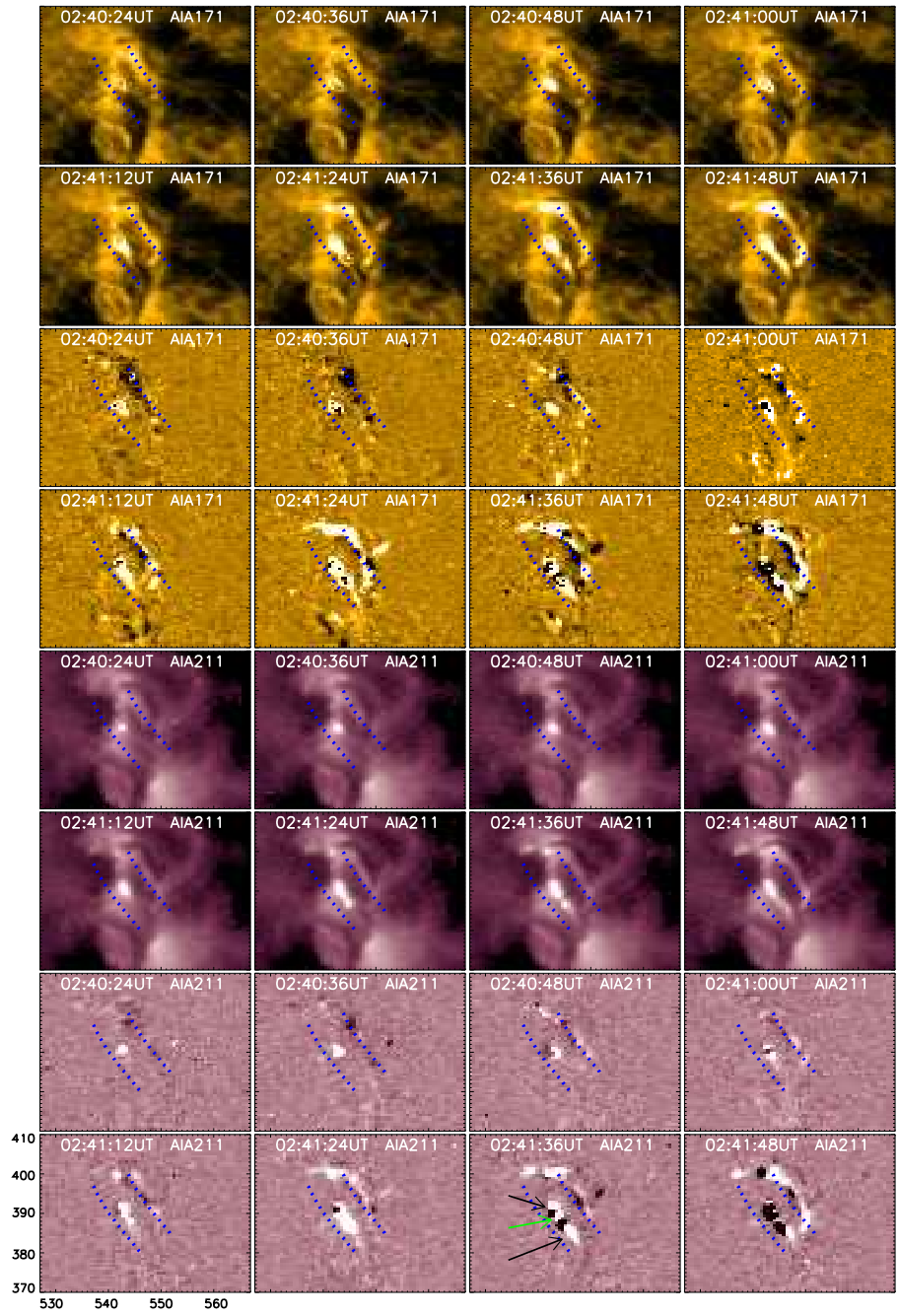

Fig. 3 Time sequence of the intensity images (*top eight and third eight panels*) and running difference images (*second eight and bottom eight panels*) at AIA 171 Å and 211 Å respectively. Each image has a same field of view as 40×40 arcsec^2. Two *blue dotted lines* outline an artificial slit same as in Fig. 1. The *black arrows* mark the bi-directional jets and the *green arrow* points the CBP core on AIA 211 Å image at 02:41:36 UT.

long the slit from northeast (bottom) to southwest (top). Therefore, the CBP core is near the middle of Y-axis, as marked by the red dotted lines. There are three pairs of the oblique streaks corresponding to the three bursts identified as three pairs of the bi-directional jets seen at all nine AIA wavelengths, although they are very weak at AIA 1700 Å, which is corresponding to the chromosphere with the lowest temperature among nine AIA wavelengths. Two jets of each burst start from the same position on the slit, and go upward and downward simultaneously. They are symmetrically distributed on the time-distance images, which is same as the bi-directional type III bursts seen on the radio dynamic spectra (e.g., Aschwanden et al. 1995; Ning et al. 2000a). Three bursts are clearly seen on the time-distance

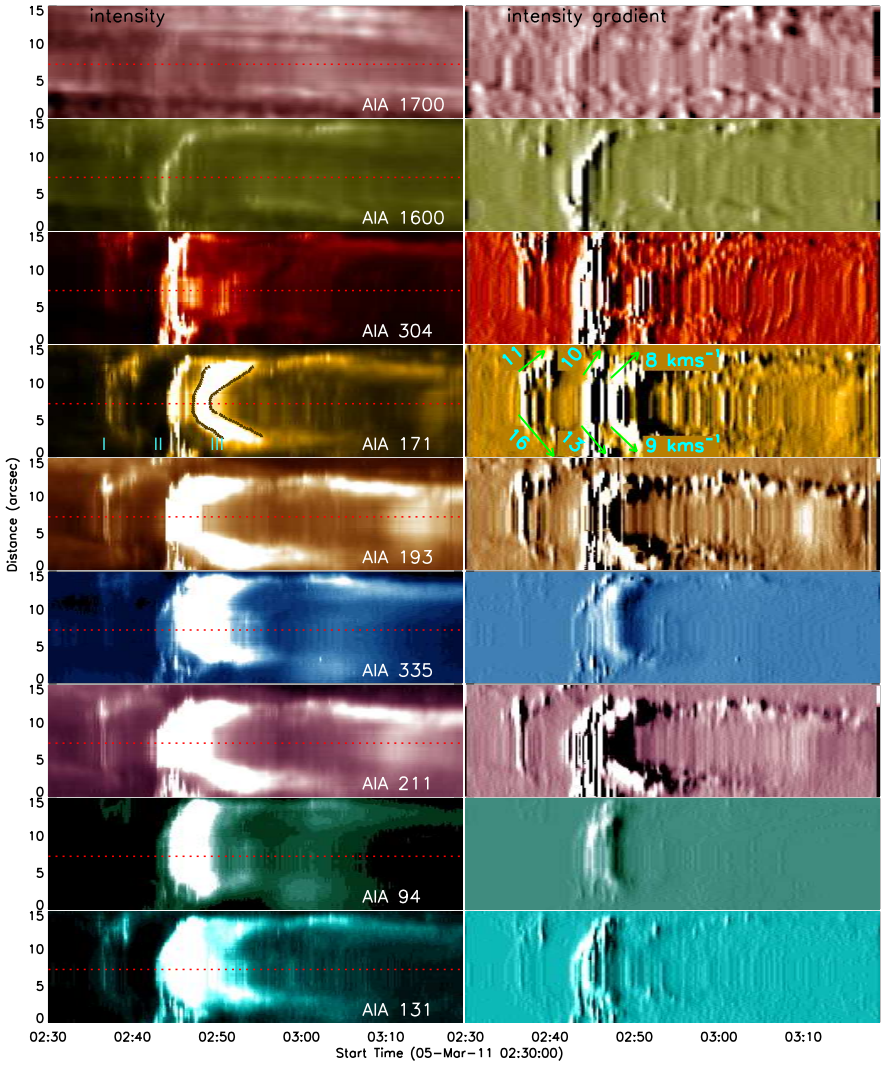

Fig. 4 Time-distance images of the intensity (*left panels*) and intensity-gradient (*right panels*) at AIA 304 Å, 171 Å, 193 Å, 211 Å, 335 Å, 94 Å, 131 Å, 1600 Å and 1700 Å respectively. The Y-axis is along the slit from northeast (*bottom*) to southwest (*top*). The *red dotted lines* represent the original position of CBP core. The light curves at the *green dashed lines* are plotted on the top panel in Fig. 5. The *triangles* mark the start and end times of the third burst at AIA 171 Å. The velocities of six jets are marked on the intensity-gradient time-distance image at AIA 171 Å.

images at AIA 171 Å, as marked by Roman numerals I, II and III. They take place at 02:36 UT, 02:42 UT and 02:50 UT respectively. Their lifetimes are increased one by one. The first burst is about 2 minutes, while the third one is about 4 minutes at AIA 171 Å. The third burst start and end times are detected on AIA 171 Å light curves each position along the slit, and they are marked by triangles in Figure 4. The second burst is clearly seen at AIA 1700 Å, 1600 Å and 304 Å, while the first and the third ones are almost not. The second and third bursts are mixed together on the raw intensity time-distance images at other five wavelengths, such as AIA 193 Å, 335 Å, 94 Å, 211 Å and 131 Å, which are the coronal lines with the temperature above 10^5 K. The light curves of four AIA channels at the green dashed lines are given in Figure 5 (top).

Figure 4 (right panels) shows the time-distance images of intensity-gradient, in which the intensity-gradient (derivative) is calculated along the X-axis (time). In this case, the signatures with weak intensities are able to be seen clearly. For example, the second burst shows weak signatures at AIA 1700 Å, and difficult to be seen at its time-distance image, while the more clear signatures are detected on the time-distance images of intensity-gradient. On the other hand, it is easy to measure the jet velocity on the time-distance images of intensity-gradient, which display the jet movement more apparently than the time-

distance images of intensity. The similar method was used before to detect the solar radio bursts or thread oscillation in a prominence (Aschwanden et al. 1995; Ning et al. 2009a,b). The jets correspond to the oblique streaks on the intensity time-distance image. After done the derivative, one jet represents a pair of a white and a dark oblique streaks. The white streak indicates the boundary where the jet intensity increases with the time, and the nearby dark one represents another boundary where the jet intensity decreases. These two streaks are consistent with the movement of both bright and dark kernels on the running difference images shown in Figure 3. According to our method, the white streaks are always followed by the dark ones on the intensity-gradient time-distance images.

Same as on the intensity time-distance images, three bursts are well displayed as three pairs of oblique streaks on the time-distance images of intensity-gradient, especially at at AIA 171 Å. The second and third bursts show their emission signatures on other eight AIA wavelengths. Figure 4 (right) also shows that the CBP starts to be bright with a roundish shape, and then it expands. This process is shown as the vertical streaks between $1''$ and $18''$ along the Y-axis at AIA 171 Å. It is shown the CBP behavior before the bi-directional jets. The streaks then become oblique, indicating the bi-directional jets moving outward. The velocities of the jets are measured as 13.5 km s^{-1}, 11.5 km s^{-1}, and 8.5 km s^{-1} for three bursts respectively. Both jets of each burst have a similar speed. Six jets have an average value of 11 km s^{-1}, which is much slower than the typical speed of X-ray jets (about 200 km s^{-1}) observed by YOHKOH (e.g., Shibata et al. 1994; Shimojo et al. 1996).

Figure 4 shows that these jets go outwards from the CBP core. Then, they stop and are continuously bright for an interval of about 20 minutes, especially at AIA 193 Å. They look like two footpoints if the bi-directional jets come from the loop top. In this case, the middle of the Y-axis is the loop top while the two footpoints are near 0 and 15 arcsec of the Y-axis in Figure 4. They correspond to the negative and positive magnetic fields on HMI image. On the intensity-gradient time-distance images, two footpoints show the bright and dark structures separately. This is the intensity oscillation, which is well seen around northeast footpoint at AIA 171 Å, 193 Å and 211 Å. In order to study this oscillation, the wavelet analysis has been done at AIA 171 Å, 193 Å, 211 Å, and also 335 Å. Figure 5 (top panels) gives their light curves along the green dashed lines on Figure 4 (left panels). There are lots of the quasi-periodic subpeaks overlying a gradual component. In order to distinguish these subpeaks from the gradual emissions, we further decompose each light curve into a higher-frequency and a lower-frequency components by the Fourier analysis. Based on the fast Fourier filtering method, the power spectrum of each light curve is splitted into a lower-frequency domain and a higher-frequency one, and the critical frequency between two domains is arbitrarily chosen to be 1/192 Hz here. The higher-frequency (quasi-periodic subpeaks) and lower-frequency (gradual background) components are obtained from the lower- and higher- frequency domains used by Inverse Fast Fourier Transform. As noted earlier, SDO/AIA has a high cadence of 12 s at 171 Å, 193 Å, 335 Å and 211 Å. Thus, the higher-frequency component refers to emission elements changing with a short timescale in the range of $24 - 192$ s, while the lower-frequency component represents emission elements changing with a longer timescale than 192 s. Figure 5 (top) also gives AIA light curves (black) with the lower-frequency components (blue) at the green dashed position in Figure 4. The higher-frequency components are shown in the middle panels, and their wavelet spectra are shown in bottom. The results show 3-min oscillations around two footpoints. This fact further proves that the bi-directional jets stop near two footpoints with the strong magnetic fields. Because the previous studies show that 3-min oscillations are often seen in the chromosphere above sunspot umbra, and are well analyzed at EUV spectral and microwave observations (Fleck & Schmitz 1991; Lites et al. 1993; Sych et al. 2012). On the other hand, the detected period of 3-min here is independence of the critical frequency 1/192 Hz in this event. In other words, we can get the same result if the critical frequency of 1/200 Hz or 1/300 Hz is chosen. The reason is that the light curves show a similar signal with a single period of 3-min in Figure 5.

3 DATA ANALYSIS

AIA multi-wavelength observations also give the ability to reconstruct the spatial images of emission measure (EM) and temperature (T) of the active region. There are more than ten methods developed to inverse the EM and T from AIA observations (Aschwanden et al. 2015). These methods basically derive from the dependence of the differential emission measure (DEM) computation, but using the different fittings of the observational data. Figure 6 shows the time-distance images of EM and T of the CBP along the slit at the 15 distinct white rectangles in Figure 1. Each rectangle has a size of 8×1 arcsec^2. The six AIA channels corresponding to the coronal temperatures, such as fluxes at 131 Å, 94 Å, 335 Å, 211 Å, 193 Å, and 171 Å, were used as initial parameters to perform the DEM fitting. The inversion method is developed from the *X-ray Telescope* (XRT) onboard *Hinode* (e.g., Hannah & Kontar 2012; Chen et al. 2012; Su et al. 2018).

There is only the third burst displayed as bi-directional oblique streaks on the time-distance images of EM and T. The third burst has large intensities at six AIA wave-

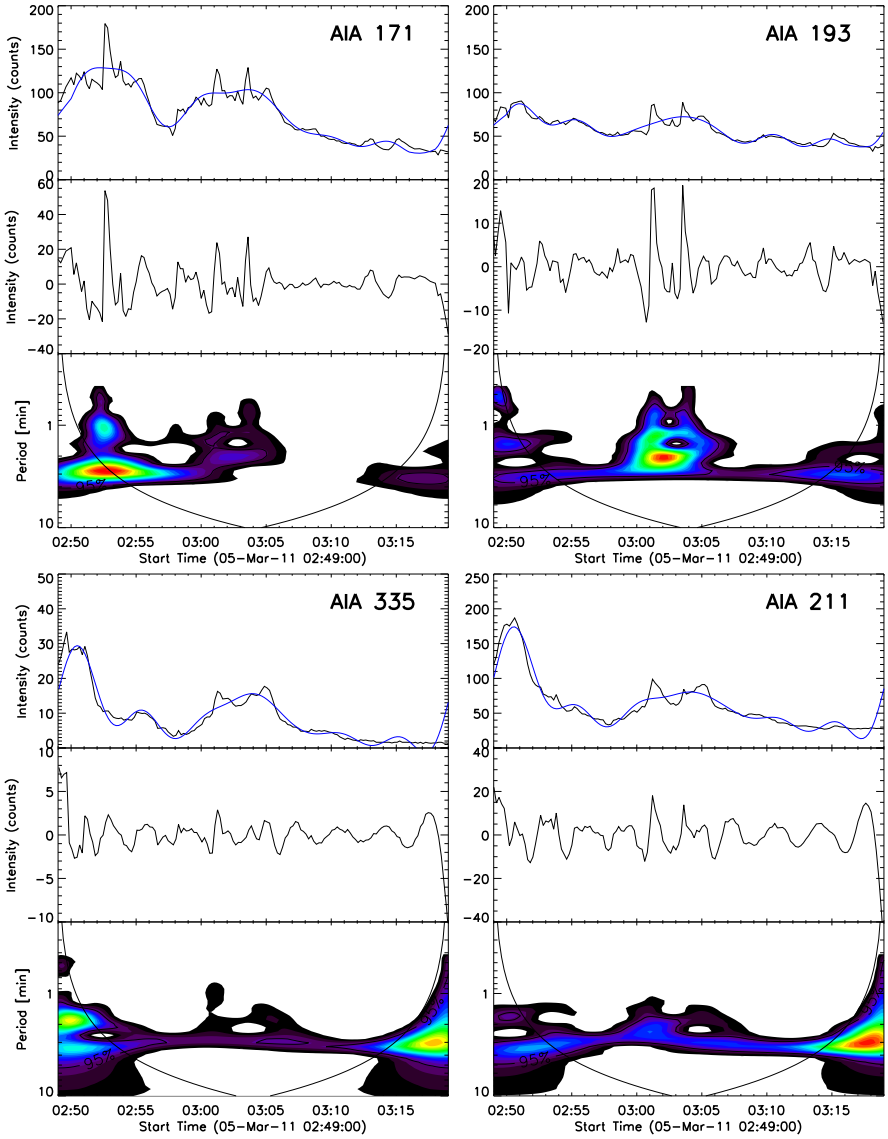

Fig. 5 *Top*: the light curves (*black*) along the *green dashed lines* in Fig. 4, and the *blue lines* are their lower-frequency components at AIA 171 Å, 193 Å, 335 Å and 211 Å respectively. *Middle*: the higher-frequency components. *Bottom*: wavelet spectra of the higher-frequency components.

lengths; i.e., F_{131}, F_{94}, F_{335}, F_{211}, F_{193}, and F_{171}. The other two bursts are too weak to invert their EM and T from observations. The third burst exhibits their EM and T movement from the CBP core (middle of the Y-axis) to outsides (top and bottom of the Y-axis) as well. Two black lines are used to trace their trajectories, and both EM and T distribution along these lines are plotted on the right panels. As the theoretical expectation, the CBP core (point c) is the magnetic reconnection region and it has a maximum EM or T along the bi-directional jets; i.e., $EM_d \leq EM_c \geq EM_b$, $T_d \leq T_c \geq T_b$. Both EM and T has a gradient distribution from the CBP core. Namely, the higher EM and T, the shorter distance to CBP core, especially on the T time-distance image. However, the point (a) has a big T than the point (b). We check the AIA observations and find that there is another CBP appearance at the same position as the point (a). This CBP is isolate and small, but its intensity contributes the inversion of EM and T in Figure 6. The DEM curves at these four points of the third burst are given in Figure 7. The red solid curve shows the best-fit DEM solution to the observed fluxes at six AIA channels. 100 Monte Carlo realizations of the data are used to estimate the DEM uncertainties, as shown by black dashes lines in each panel. Each position shows a wide temperature range between 0.3 MK and 10 MK ($5.5 \leq \log T \leq 7.0$). The average values of EM and T are given.

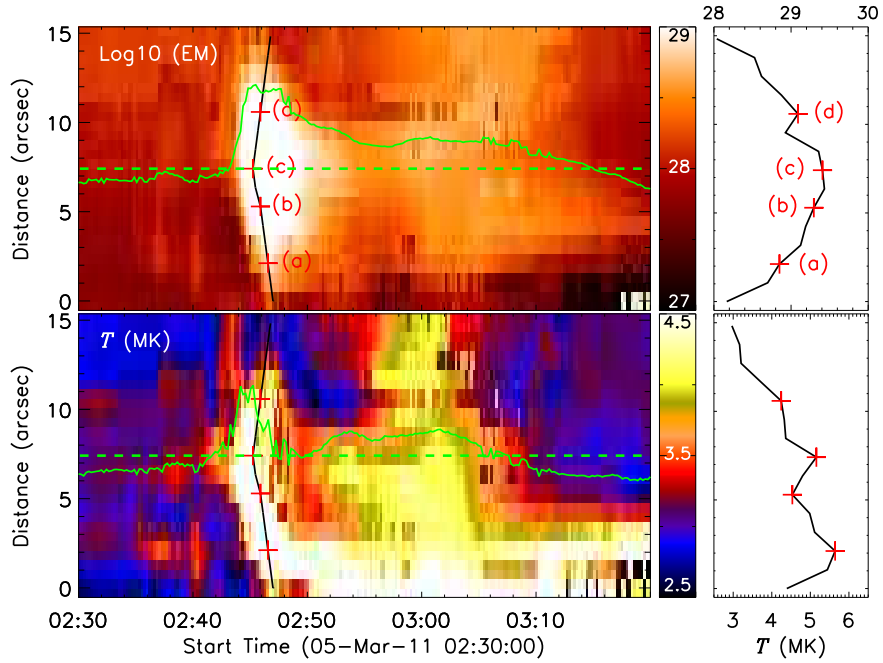

Fig. 6 *Left*: time-distance images of EM and T using the *Hinode*/XRT method along each of the 15 *white rectangles* marked in Fig. 1 from northeast (*bottom*) to southwest (*top*). The *green line* shows the time evolution of EM and T at 7 arcsec on the Y-axis. The DEM curves at four positions marked by *pluses* (a, b, c, d) are given in Fig. 7. *Right*: EM and T distributions along two *black oblique lines* (the third bi-directional jets).

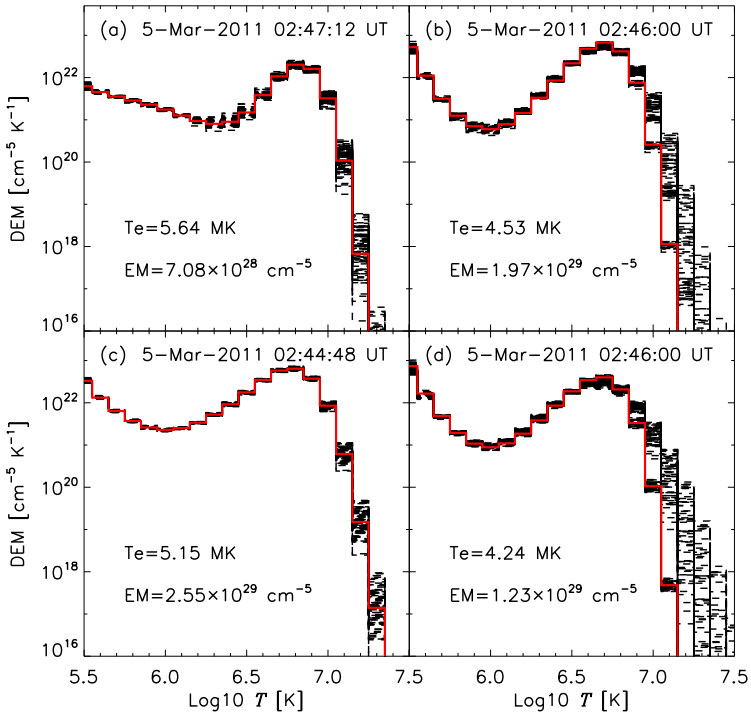

Fig. 7 DEM curves at the four positions along the third bi-directional jets. *Black dashed* and *red lines* are 100 Monte Carlo realizations of the data and the best-fit DEM distributions respectively.

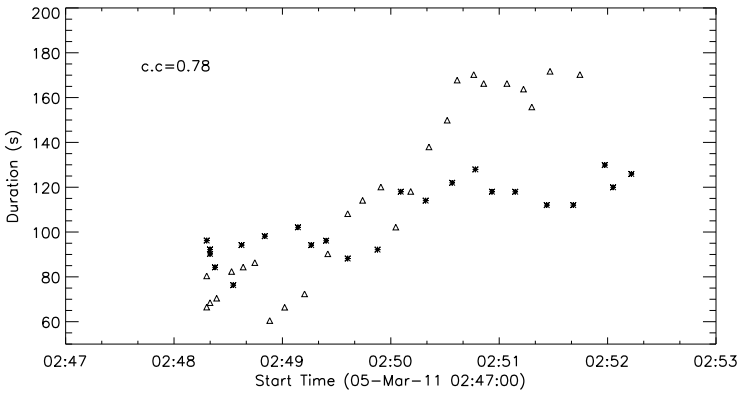

Fig. 8 Measurements of the jet durations dependence on the peak times. The *triangles* and *asterisks* correspond to the upward and downward jets of the third burst at AIA 171 Å in Fig. 4.

Meanwhile, the jets are the emission signatures of the plasma outflows moving from the acceleration region. Observationally, the jet shifts its maximum peak with the time, indicating the jet movement, such as oblique streaks shown in Figure 4. On the other hand, the jet durations are expected to increase regularly and continuously on its trajectories after left the acceleration region. This is because of the dispersion (δv) of the plasma speed. The δv results into the spacial expansion of the jet with the time, such as

$$L_{\rm jet} \sim L_0 + \delta v \times \delta t$$

where δv is speed dispersion and δt is elapsed time after jet (outflow) left the acceleration region. When $\delta t = 0$, $L_{\rm jet} = L_0$, L_0 is the original length of jet at the acceleration region. Thus, the jet scale would continuously increase with the elapsed time, and the jet duration could regularly increase with the elapsed time. Because the jet duration is proportional to the jet scale. Figure 8 plots the jet durations dependence on the peak times at AIA 171 Å. The triangles and asterisks represent upward and downward jet durations of the third burst respectively. As we expected, the jet durations increase regularly along with their peak times, which are measured as the times with the maximum 171 Å flux at each Y position in Figure 4. This indicates that the bi-directional jets could be radiate by the plasma outflows expanding their scale after leaving the acceleration region. This finding is consistent with the relation between the duration of type III bursts and their peak times (e.g., Hillaris et al. 1988; Ning et al. 2000b).

4 DISCUSSIONS AND CONCLUSIONS

We analyzed the bi-directional jets in a CBP observed by SDO/AIA at nine wavelengths on 2011 March 5 in this paper. Traditionally, a CBP is coronal compact brightenings in coronal holes or quiet sun regions. The event studied here is not a classical CBP but active region bright core with a size comparable to a CBP, like a bright point in the active region moss (Tripathi et al. 2008, 2010). Our observations show that this event is a small-scale loop system in active regions that have similar size as a traditional CBP, and it might also shed light on the physics of a traditional CBP.

This CBP exhibits its brightness flashes three times on the light curves. AIA imaging observations show that they are three bursts intermittently, and each burst is identified as a pair of bi-directional jets, which starts from the looptop and moves towards two footpoints. In order to analyze these bi-directional jets, we use an artificial slit with a width of $8''$ to cover the whole CBP. After integration the fluxes along the slit width, we get the brightness time-distance images at AIA nine wavelengths. As expected, the bi-directional jets are identified as the bi-directional oblique streaks on the time-distance images of various AIA wavelengths. The bi-directional jets almost start at the CBP core near the loop top, and move outwards at the opposite directions. The jets have an average speed of about 11 km s^{-1}, which is much slower than the X-ray jets. These jets stop around the loop footpoints, which are bright for a period about 20 minutes after the jets. High cadence observations show 3-min oscillation around these two footpoints.

Our observations show the typical characteristics of the bi-directional jets. First, the jets come from the CBP core around the loop top. Second, they are symmetrically seated outsides the CBP core, and move outward the opposite directions. Both jets exhibit as the oblique streaks symmetrically distributed on the time-distance images. Third, their velocities are comparable. In brief, they have the similar shapes, similar speeds and similar behaviors, but the opposite directions. Meanwhile, we find that both EM and T display a gradient distribution from the CBP core to two sides. The jets increase their durations with the peak times. It is reminiscent of the bi-directional plasma

outflow after the magnetic reconnection. We explain that these bi-directional jets are the observational evidences of the bi-directional plasma outflows produced by the magnetic reconnection model. In other words, our findings support the magnetic reconnection model of the CBP. The bi-directional jets seem to start from the loop top, then expand and move toward two footpoints, indicating the magnetic reconnection occurrence around the loop top. Namely, we suppose that there is a loop system connecting the positive and negative fields in this case, and the event started to erupt on the loop top due to magnetic reconnection took place there, possibly reconnection between the emergence loops and pre-existing and overlying fields (Priest et al. 1994; Mou et al. 2016; Mou et al. 2018), or possibly reconnection on the loop top due to the convergence motion (Mou et al. 2016), or due to a cusp shape field (Masuda et al. 1994). However, no such convergence or a cusp shape is found from magnetic and optic observations. We try to use the difference image of magnetic field in Figure 1(d) to look for the magnetic emergence or cancelation or convergence beneath the event. It seems that the event region does change its magnetic field, but such changes are comparable with the noise level in Figure 1(d). It is possible that the magnetic structures evolve quickly with a shorter timescale or more weakness than the present instrument resolution. As noted earlier, AIA 171 Å images show that a thermal loop appears during the event, which supports our hypothesis that three bursts are possible resulting from intermittent reconnection on this loop top. Thus, the bi-directional jets produced and started from the loop top toward their footpoints along these loops. On ther other hand, there is another possibility that the bi-directional jets in this event are like flows along the post-reconnection loops, because the reconfiguration of field lines in a magnetic system could result in transferring of mass between different loops and movement along the loops (Huang et al. 2018).

The magnetic reconnection model is also well used to interpret the transition region explosive events (Innes et al. 1997; Chae et al. 1999), the X-ray jets (Shimojo et al. 1996), and bi-directional type III bursts in solar flares (Aschwanden et al. 1995; Ning et al. 2000a). However, their observational speeds have a big gap, for example, 11 $\mathrm{km\,s^{-1}}$ for the jets in this paper, about 100 $\mathrm{km\,s^{-1}}$ for the outflows of the explosive events, and about 200 $\mathrm{km\,s^{-1}}$ for X-ray jets, about one third of light speed ($\sim 10^5$ $\mathrm{km\,s^{-1}}$) for the electron beams of type III bursts. Theoretically, the outflow speed is related to the local plasma density and magnetic strength (i.e., Alfvén speed), which are dependent on the height of the solar atmosphere. The big gap of outflow speeds suggests that the reconnection takes place at various layers (e.g., Shibata et al. 2007). Such slow speed of the bi-directional jets in this paper probably suggests the magnetic reconnection in the lower coronal layer with a very weak magnetic field and a high plasma density. Meanwhile, three bursts take place intermittently and show a quasi-periodicity of 7 minutes. Actually, the periodicity is also well observed in other reconnection events, such as $3-5$ minutes for the explosive events (e.g., Ning et al. 2004; Li 2019), tens minutes for X-ray jets (Zhang et al. 2012), and 2 seconds for type III bursts (Aschwanden et al. 1995; Ning & Guo 2014; Li et al. 2016). Such big gap of the periods would support the assumption that the magnetic reconnection could be modulated by the waves with various periods (e.g., Chen & Priest 2006).

AIA observations show that not all the three bursts can be seen at all nine AIA wavelengths, which indicates that the jet plasma has various temperatures. As noted earlier, three bursts are well seen at AIA 171 Å, while only one or two bursts show the signatures at other eight AIA wavelengths. Only the second burst is seen at all nine AIA wavelengths, i.e., from AIA 1700 Å to 131 Å, which correspond a wide temperature range between 10^3 K and 10^6 K. Three bursts are more bright at the coronal lines such as AIA 335 Å, 94 Å, and 131 Å than the chromospherical lines, such as AIA 1600 Å and 1700 Å. This fact suggests that the hot plasma as well as the corona is still the main component in the jets. The image observations combined with EUV spectra could be helpful to study the jet plasma temperatures.

Acknowledgements This work is funded by the National Natural Science Foundation of China (NSFC, Grant Nos. 11173062, 11333009 and 11573072) and Laboratory (No. 2010DP173032).

References

Alexander, C. E., Del Zanna, G., & Maclean, R. C. 2011, A&A, 526, A134
Aschwanden, M. J., Boerner, P., Caspi, A., et al. 2015, Sol. Phys., 290, 2733
Aschwanden, M. J., Benz, A. O., Dennis, B. R., & Schwartz, R. A. 1995, ApJ, 455, 347
Carmichael, H. 1964, NASA Special Publication, 451
Chae, J., Qiu, J., Wang, H., & Goode, P. R. 1999, ApJ, 513, L75
Chen, P. F., Priest, E. R. 2006, Sol. Phys., 238, 313
Cheng, X., Zhang, J., Saar, S. H., Ding, M. D. 2012, ApJ, 761 62
Cirtain, J. W., Del Zanna, G., DeLuca, E. E., Mason, H. E., Martens, P. C. H., Schmelz, J. T. 2007, ApJ, 655, 598
Dere, K. P. 2008, A&A, 491, 561
Fleck, B., & Schmitz, F. 1991, A&A, 250, 235
Fu, Q., Kundu, M. R., & Schmahl, E. J. 1987, Sol. Phys., 108, 99
Golub, L., Krieger, A. S., Harvey, J. W., & Vaiana, G. S. 1977, Sol. Phys., 53, 111

Golub, L., Krieger, A. S., Silk, J. K., Timothy, A. F., & Vaiana, G. S. 1974, ApJL, 189, L93
Fang, F., Fan, Y., & McIntosh, S. W. 2014, ApJL, 789, L19
Fu, Q., Kundu, M. R., & Schmahl, E. J. 1987, Sol. Phys., 108, 99
Habbal, S.R., Ronan, R. S., Withbroe, G. L., Shevgaonkar, R. K., Kundu, M. R. 1986, ApJ, 306, 740
Habbal, S. R., Withbroe, G. L., Dowdy, J. F. Jr. 1990, ApJ, 352, 333
Habbal, S. R., & Withbroe, G. L. 1981, Sol. Phys., 69, 77
Harvey, K. L., Strong, K. S., Nitta, N., & Tsuneta, S. 1994, Solar Active Region Evolution: Comparing Models with Observations, 68, 377
Hannah, I. G., & Kontar, E. P. 2012, A&A, 539, A146
Hillaris, A., Alissandrakis, C. E., & Vlahos, L. 1988, ApJ, 195, 301
Hirayama, T. 1974, Sol. Phys., 34, 323
Huang, Z. 2018, ApJ, 869, 175
Huang, Z., Li, B., & Xia, L. 2019a, Solar-Terrestrial Physics, 5, 58
Huang, Z., Li, B., Xia, L., et al. 2019b, ApJ, 887, 221
Huang, Z., Madjarska, M. S., Doyle, J. G., et al. 2012, A&A, 548, A62
Huang, Z., Mou, C., Fu, H., et al. 2018, ApJ, 853, L26
Innes, D. E., Inhester, B., Axford, W. I., & Wilhelm, K. 1997, Nature, 386, 811
Innes, D. E., Genetelli, A., Attie, R., et al. 2009, A&A, 495, 319
Innes, D. E., McIntosh, S. W., & Pietarila, A. 2010, A&A, 517, L7
Kamio, S., Curdt, W., Teriaca, L., & Innes, D. E. 2011, A&A, 529, A21
Kariyappa, R., & Varghese, B. A. 2008, A&A, 485, 289
Kariyappa, R., Deluca, E. E., Saar, S. H., et al. 2011, A&A, 526, A78
Kopp, R. A., & Pneuman, G. W. 1976, Sol. Phys., 50, 85
Koutchmy, S., Hara, H., Suematsu, Y., & Reardon, K. 1997, A&A, 320, L33
Krieger, A. S., Vaiana, G. S., & van Speybroeck, L. P. 1971, Solar Magnetic Fields, 43, 397
Lemen, J. R., Title, A. M., Akin, D. J., et al. 2012, Sol. Phys., 275, 17
Lites, B. W., Rutten, R. J., & Kalkofen, W. 1993, ApJ, 414, 345
Longcope, D. W., Kankelborg, C. C., Nelson, J. L., & Pevtsov, A. A. 2001, ApJ, 553, 429
Li, D., Ning, Z. J., & Wang, J. F. 2013, New Astronomy, 23, 19
Li, D., & Ning, Z. 2012, Ap&SS, 341, 215
Li, D., Ning, Z., & Su, Y. 2016, Ap&SS, 361, 301
Li, J.-W., & Li, H. 2010, RAA (Research in Astronomy and Astrophysics), 10, 696
Li, D. 2019, RAA (Research in Astronomy and Astrophysics), 19, 67
Liu, W., Chen, Q., & Petrosian, V. 2013, ApJ, 767, 168
Madjarska, M. S., Doyle, J. G., Teriaca, L., & Banerjee, D. 2003, A&A, 398, 775
Masuda, S., Kosugi, T., Hara, H., et al. 1994, Nature, 371, 495
Moore, R. L., Cirtain, J. W., Sterling, A. C., et al. 2010, ApJ, 720, 757
Moreno-Insertis, F., Martinez-Sykora, J., Hansteen, V. H., et al. 2018, ApJL, 859, L26
Mou, C., Huang, Z., Xia, L., et al. 2016, ApJ, 818, 9
Mou, C., Madjarska, M. S., Galsgaard, K., et al. 2018, A&A, 619, A55
Ning, Z., Cao, W., & Goode, P. R. 2009a, ApJ, 707, 1124
Ning, Z., Cao, W., Okamoto, T. J., Ichimoto, K., & Qu, Z. Q. 2009b, A&A, 499, 595
Ning, Z., Fu, Q., & Lu, Q. 2000a, Sol. Phys., 194, 137
Ning, Z., Yan, Y., Fu, Q., & Lu, Q. 2000b, A&A, 364, 793
Ning, Z., & Guo, Y. 2014, ApJ, 794, 79
Ning, Z., Innes, D. E., & Solanki, S. K. 2004, A&A, 419, 1141
Pariat, E., Antiochos, S. K., & DeVore, C. R. 2009, ApJ, 691, 61
Petschek, H. E. 1964, NASA Special Publication, 425
Priest, E. R., Parnell, C. E., & Martin, S. F. 1994, ApJ, 427, 459
Podgorny, A. I., & Podgorny, I. M. 2000, Astronomy Reports, 44, 407
Scherrer, P. H., Bogart, R. S., Bush, R. I., et al. 1995, Sol. Phys., 162, 129
Skokić, I., Brajša, R., Sudar, D., et al. 2019, ApJ, 877, 142
Sturrock, P. A. 1966, Nature, 211, 695
Strong, K. T., Harvey, K., Hirayama, T., Nitta, N., Shimizu, T., & Tsuneta, S. 1992, PASJ44, L161
Sheeley, N. R., Jr., & Golub, L. 1979, Sol. Phys., 63, 119
Shibata, K., Ishido, Y., Acton, L. W., et al. 1992, PASJ, 44, L173
Shibata, K., Nitta, N., Strong, K. T., et al. 1994, ApJ, 431, L51
Shibata, K., Nakamura, T., Matsumoto, T., et al. 2007, Science, 318, 1591
Shimojo, M., Hashimoto, S., Shibata, K., et al. 1996, PASJ, 48, 123
Su, Y., Veronig, A. M., Holman, G. D., et al. 2013, Nature Physics, 9, 489
Su, Y., Veronig, A. M., Hannah, I. G., et al. 2018, ApJL, 856, L17
Sych, R., Zaqarashvili, T. V., Nakariakov, V. M., Anfinogentov, S. A., Shibasaki, K., & Yan, Y. 2012, A&A, 539, A23
Tian, H., Xia, L.-D., & Li, S. 2008, ApJ, 489, 741
Tripathi, D., Mason, H. E., Young, P. R., et al. 2008, A&A, 481, L53
Tripathi, D., Mason, H. E., Del Zanna, G., et al. 2010, A&A, 518, A42
Ueda, K., Kano, R., Tsuneta, S., & Shibahashi, H. 2010, Sol. Phys., 261, 77
Webb, D. F., Martin, S. F., Moses, D., & Harvey, J. W. 1993, Sol. Phys., 144, 15
Yokoyama, T., & Shibata, K. 1995, Nature, 375, 42
Zhang, J., Kundu, M. R., & White, S. M. 2001, Sol. Phys., 198, 347
Zhang, Q. M., Chen, P. F., Guo, Y., Fang, C., & Ding, M. D. 2012, ApJ, 746, 19